Design and Analysis of Beam Separator Magnets for 3rd Generation Aberration Compensated PEEMs ⋆

Y. K. Wu [a,b] , D. S. Robin [b] , E. Forest [b,c] , R. Schlueter [b]
S. Anders [d] , J. Feng [b] , H. Padmore [b] , D. H. Wei [b,e]

[a] *Department of Physics, Duke University, Durham, NC 27708, USA*

[b] *Lawrence Berkeley National Lab, 1 Cyclotron Road, Berkeley, CA 94720, USA*

[c] *High Energy Accelerator Research Organization, 1-1 Oho, Tsukuba, Ibaraki 305-0810, Japan*

[d] *IBM Almaden Research Center, 650 Harry Road, San Jose, CA 95120*

[e] *Synchrotron Radiation Research Center, 1 R&D Road, Science-Based Industrial Park, Hsinchu, Taiwan 30077*

Abstract

A state of the art x-ray photoemission electron microscope (PEEM2) is operational at the Advanced Light Source at a resolution of typically 50 nm for a range of chemical and magnetic surface studies. A new microscope, PEEM3, is under development with an aim of achieving a resolution of 5 nm and more than an order of magnitude increase in transmission at the nominal resolution of PEEM2. The resolution and flux improvement is realized by providing geometric and chromatic aberration compensations in the system using an electron mirror and a beam separator magnet. The nearly aberration-free design of the beam separator is critical to the performance of 3rd generation PEEMs. In this paper, we present the optics design model, optimal operation parameters, analyses of aberration impact, as well as the mechanical alignment tolerance for PEEM3 separator prototypes. In particular, we emphasize the importance of a new semi-analytical approach to design complex charged particle optics using the truncated power series algebra (TPSA). Because of its ability to compute high order aberrations, this approach allows systematic and comprehensive analyses of any charged particle optics systems with analytical electric and magnetic fields.

Key words: beam separator, electron microscope, electron optics, aberrations
PACS: 07.78, 41.85, 42.15.F, 41.75

1 Introduction

Photoemission electron microscopes (PEEMs) have been developed since the 1930's [1,2] to study the surface and thin film properties of various materials. Like the first generation systems, the second generation PEEMs do not have built-in aberration correction optics. However, with much improved electron optics and the assistance of an energy filter or an energy selecting aperture, much improvement in the spatial resolution has been achieved in the second generation PEEMs such as PEEM2 at the Advanced Light Source (ALS), Berkeley National Laboratory. Operated at beamline 7.3.1.1 since 1998 [3], PEEM2 is an x-ray PEEM (XPEEM) for studying magnetic thin-films, polymers and other thin-film material and interfaces. The best resolution achieved by PEEM2 was 20 nm by imaging a discharge track on a $LaFeO_3$ sample at the LaM_5 edge [3]. The exposure time was 60 seconds due to a low electron transmission limited by the resolution boosting aperture located at the back focal plane of one of the lenses. Routinely PEEM2 has been operated with a typical spatial resolution of 50 nm to 100 nm with a electron transmission of 2–5%. However, a higher spatial resolution and a larger electron transmission are critical for many important research areas: (a) research in ferromagnetic and anti-ferromagnetic thin films, in particular, thin multi-layered or nanostructured materials, in which the ability to obtain information on buried interfaces is essential; (b) research in polymer systems on a nanometer length scale, in confined geometries, on patterned surfaces and near interfaces. The higher resolution and flux requirements can only be achieved with aberration correction optics built into a PEEM. At the ALS, we are developing such an aberration corrected system – PEEM3, one of a few third generation PEEM systems capable of addressing the above research needs [4]. Another 3rd generation PEEM, SMART (SpectroMicroscope for All Relevant Techniques) in Germany, has been developed as a ultrahigh-resolution spectromicroscope for BESSY II [5–8]. Unlike SMART where a combined electric and magnetic objective lens is employed, PEEM3 uses an all-electric objective lens to optimize the performance in studying the magnetic surfaces and interfaces. However, a major difference between PEEM3 and SMART is that PEEM3 is designed as a dedicated microscope to optimize the full flux performance while SMART is a more complex system with a large number of operation modes. For example, SMART employs an advanced narrow-band Omega energy filter to function as a dual spectro-microscope. PEEM3 is designed for a more restrictive operation in which spectroscopic information is obtained only from monitoring the change in electron emission as a function of photon energy, not from analyzing

⋆ Work supported by the Director, Office of Energy Research, Office of Basic Energy Sciences, Material Sciences Division, U.S. Department of Energy, under Contract No. DE-AC03-76SF00098

[1] Corresponding author. E-mail: wu@fel.duke.edu.

the energy of photoemitted electrons. However, the power of this x-ray absorption imaging method allows a huge range of complex materials problems to be addressed and in reality will not restrict the types of scientific questions that can be studied.

The interaction of a photon with a sample leads to the generation of primary photoelectrons. These photoelectrons, together with Auger electrons formed as a result of filling the core hole created by photoemission suffer electron scattering within the solid, resulting in an electron kinetic energy spectrum that is characterized by a secondary electron distribution peaked at a few eV and extending to 10's of eV, with weak primary photoemission peaks superimposed. Because of the mismatch of the photon penetration (typically 0.2 microns for 1 keV photons in a transition metal) and low energy electron scattering lengths (typically 2 - 3 nm), most of the electrons emitted from the sample are in the low energy secondary electron distribution. Correction of the focusing errors caused by the chromatic nature of the source and the chromatic aberrations of the accelerating field and lenses is one of the primary goals of PEEM3.

The aberration correction mechanism in 3rd generation PEEMs is provided by an electrostatic tetrode mirror in combination with a magnetic beam separator (see Fig. 1). The tetrode mirror corrects the spherical and chromatic aberrations of the system dominated by the frontend elements of the accelerating gap and the objective lens. The beam separator bends the electron beam into and out of the tetrode mirror, making the aberration correction possible by the mirror. To archive a high spatial resolution, the separator magnet needs to be designed nearly free of dominant aberrations, which is realized in a highly symmetric design of the magnet.

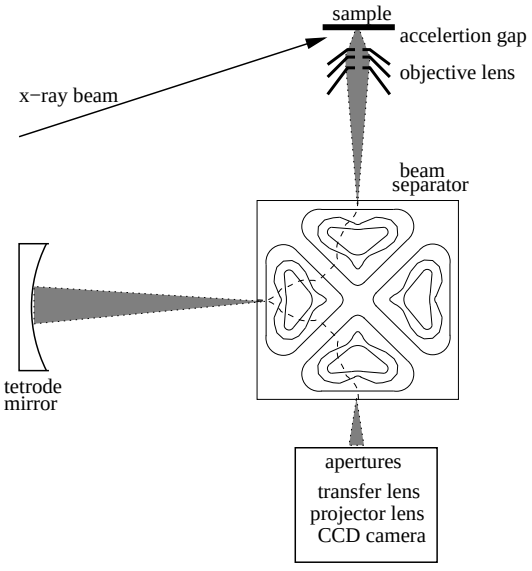

Fig. 1. A schematic layout of the PEEM3 optics including the acceleration gap, objective lens, beam separator, and tetrode mirror.

PEEM3 is designed to operate in two main modes: a high resolution mode and a high flux mode. In the high resolution mode, PEEM3 is designed to achieve a spatial resolution of 5 nm at a flux level of a few percent comparable to that of PEEM2 at 50–100 nm resolutions. In the high flux mode, an electron transmission up to 90% is to be realized at a spatial resolution of 40–50 nm. In addition, PEEM3 is expected to work with samples of various sizes with field sizes from microns to 10's of microns. The resolution goals of PEEM3 set an up-limit for the amount of aberrations that can be tolerated in the beam separator. Noting that the PEEM3 resolution is greatly improved with a reduced electron flux, we set the following conservative aberration requirements for passing through a quadrant of the separator: (1) < 1 nm for a 1 μm $\times$ 1 μm field of view (90% electron throughput); (2) < 5 nm for a 10 μm $\times$ 10 μm field of view (90% electron throughput); in terms of its contribution to the sample resolution.

2 Modeling Beam Separators

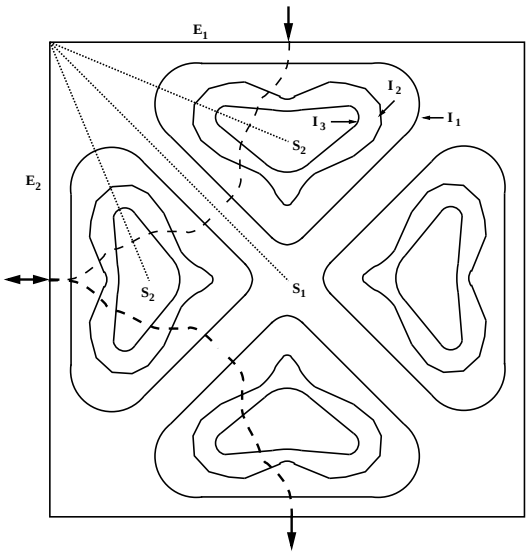

Fig. 2. A schematic layout of the beam separator. Two symmetry planes S_1 and S_2 are indicated by doted lines and the beam trajectory by the dashed line.

Like the SMART separator, the PEEM3 separator employs a square layout with a double mirror symmetry for each quadrant of the magnet (see Fig. 2). Starting from the entrance plane, E_1, along its trajectory, the electron beam encounters symmetry planes, S_2, S_1, and S_2 when its direction is bent by 22.5, 45, and 67.5 degrees respectively. The beam exits the separator at the exit plane, E_2. In the separator, there are four yoke surfaces partitioned by three looped coils. The zero magnetic field condition outside of the separator requires the currents in the triplet coils to satisfy the equation: $I_1 + I_2 + I_3 = 0$. We elect to choose $I_1 = I_3 = I$ and $I_2 = -2I$.

Fig. 3 shows the cross-section of the separator along the reference trajectory of the beam. Three sets of coils are buried in grooves separated by equi-potential pole surfaces. Accurate analytic presentation of the magnetic field is critical for computing high order aberrations. Through the proper design of the coil triplet, the straight piece of the groove perpendicular to the beam direction can be made much larger than the size of the gap. Consequently, the magnetic field across the groove area can be modeled analytically as a 2D field using the conformal map technique.

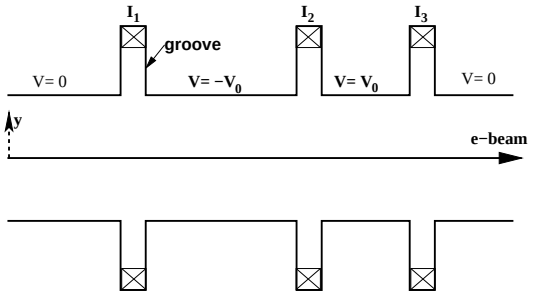

Fig. 3. Beam separator cross-section along the electron beam direction.

In PEEM3 separator design, we use this localized 2D analytic magnetic field model. In contrast, the magnetic field in the SMART separator is calculated using a semi-analytical charge simulation method [7]. While the charge simulation is capable of better describing the 3D effect of the magnetic field, the simpler 2D field model provides adequate description of the field in the separator. This has been demonstrated by the very good agreement of computed separator current and field values as well as on-axis aberration terms between these two different field models used by SMART and PEEM3 (see Section 3).

It is well known that two sextupoles separated by a telescopic optics with a magnification of -1 have most of their second-order aberrations cancelled. We refer to such a telescopic transformation as a $(-I)$-transformation. The remaining second order terms are related to the scaled transverse momenta (beam angles) and fractional energy spread: $p_{x,y}\delta$ (the chromaticity terms in the accelerator language). In fact, due to the double symmetry present in the separator, a large number of higher order aberrations are also cancelled. In other words, this highly symmetric system is capable of aberration self-correction. The remaining main task is to design such a symmetric optical system and to perform analyses to ensure the remaining aberrations are small compared with the resolution requirement.

Truncated power series algebra (TPSA) technique [9,10] allows computation of aberrations to any high orders if the electric and/or magnetic field is known to the corresponding orders. The PEEM3 separator optics design code is developed using a Fortran 90 overloaded TPSA software package, FPP [11]. Because of the natural compensation scheme built into the symmetric design, only linear optics design is required. There are a total of six constraints: (a)

two $(-I)$-transformation in both horizontal and vertical planes (4 constraints due to the mirror symmetry); (b) the incoming beam is bent by 90 degrees upon exiting the magnet (1 constraint); (c) zero dispersion at the S_2 symmetry plane (1 constraint). We use the following six variables for fitting: (a) three groove positions; (b) two groove angles (the first groove is fixed, always parallel to the edge of the magnet); (c) the current in the triplet-coil sets, I. The Newton search method is used to find the linear optics solution for the separator. After the solution has been found, a TPSA map is then generated to include high order aberrations. Ray-tracing shows that 4th order TPSA maps are rather adequate for consistent calculations of on-axis and off-axis beam distributions.

The rigorous study of the separator impact on PEEM3 resolution can only be performed after the rest of the PEEM3 system including the frontend and correction mirror is fully developed. In this preliminary study of separator prototypes, we utilize a simplified PEEM3 model from the emission plane of the sample to the exit after one quadrant of the separator. The acceleration gap and objective lens are modeled as linear elements, the only nonlinear element in this model is a 4th order TPSA map representing aberrations in one quadrant of the separator. Ray-tracing is then performed to compute the electron beam distribution at the image plane at the exit of the separator for a given point source located either on-axis or at a corner of the field of view. The horizontal and vertical image sizes are determined by a radius containing 68% of the beam intensity in the respective directions as used in the SMART project [7]. Finally, the image size scaled by the frontend magnification gives the "effective sample resolution" of this simplified model system.

3 Optimal Beam Separator for PEEM3

Using the magnetic field and optics design models outlined in the previous section, beam separators with various physical sizes can be designed and their impact on resolution fully analyzed. Besides its size, the performance of a given separator also depends on the choice of the frontend system parameters such as the acceleration gap voltage and magnification. In this section, we focus on design and operation considerations for the PEEM3 separator.

The overall resolution of an optics system is determined by two key factors: the quality of the charged particle beam and the aberrations in the system. This point can be illustrated using the dominating on-axis aberration terms of the separator:

$$x_2 \approx x_{\alpha\kappa}\, p_{x1}\, \delta, \quad y_2 \approx y_{\beta\kappa}\, p_{y1}\, \delta + y_{\beta\beta\beta}\, p_{y1}^3, \tag{1}$$

where x and y denote the horizontal and vertical coordinates, α and β, horizontal and vertical angles, κ, fractional energy spread, and subscripts, 1 and 2, entrance and exit locations of the separator respectively. The electron positions after the separator, x_2, y_2, depend on the incoming ray angles expressed in terms of the scaled transverse momenta, p_{x1}, p_{y1}, and the relative fractional energy deviation, δ, as well as the magnitude of the aberration coefficients, $x_{\alpha\kappa}$, $y_{\beta\kappa}$, and $y_{\beta\beta\beta}$. Consequently, a point source will produce an image with finite transverse sizes after the separator and the sizes of this image, $\Delta x, \Delta y$, will depend on the angular and energy spreads of the incoming beam as well as the magnitude of the aberration coefficients of the separator. It is obvious that the optimal performance of the separator can be achieved through both improving beam quality and reducing aberrations in the separator.

3.1 Frontend System

For many surface materials of interest, the secondary electron distribution can be effectively modeled by the following function [12]

$$\frac{dN}{dE_k} \propto \frac{E_k}{(E_k + W)^4} \tag{2}$$

where dN is the number of electrons in a kinetic energy span dE_k, and W is the work function of the surface. The work function, W, splits the total electron distribution in two equal portions: 50% of electrons with emission energies lower than W and the other 50% higher than W. In this study, the work function is chosen to be 5 eV.

The quality of the electron beam coming into a PEEM is determined by its frontend system of the acceleration gap and objective lens. A higher acceleration gap voltage will help reduce both the angular spread and the fractional energy spread of the beam. Using a simple transfer model which assumes that the gap is very small so that the transverse momentum does not change across the gap, we have the following relationships for the scaled transverse momentum, $p_{x,y}$, and the fractional energy deviation, δ:

$$p_{x,y} \approx \sqrt{\frac{E_K}{U_g}}, \qquad \delta = \frac{E_K}{U_g},$$

where U_g is the energy gain in the gap by the electron, E_K, the kinetic energy of the election coming off the sample, and $E_K << U_g$. A large gap voltage is desirable for improving PEEM3 resolution. However, in reality, the maximum gap voltage is limited by sample breakdown at a high electric gradient. For PEEM3, we elect to use the same standard gap voltage as in PEEM2: 20 kV across the 2 mm gap.

The frontend magnification also plays important roles in determining the sample resolution: (1) the angular spread of the beam coming into the separator is reduced by magnification; (2) the same image size corresponds to a smaller sample area due to magnification. Because the on-axis aberration of the separator is dominated by terms, $p_x\delta$ and $p_y\delta$, we expect that the impact on the sample resolution due to the separator will scale proportionally to the inverse square of magnification. Table 1 shows computed sample resolution due to various frontend magnifications for a 90×90 cm beam separator. As expected the horizontal sample resolution is improved by a factor of 9.7 when increasing the magnification from -10 to -30. We also notice that the vertical improvement is less than the horizontal, which is due to more profound partial cancellation between the $p_y\delta$-term and p_y^3-term at a lower magnification.

Frontend Magnification	Image Size (nm) (x, y)	Effective Sample Resolution (nm)	Resolution Improvement
-10	$(36.6, 126)$	$(3.7, 12.6)$	$(1, 1)$
-20	$(17.1, 74.8)$	$(0.85, 3.74)$	$(4.4, 3.4)$
-30	$(11.4, 51.5)$	$(0.38, 1.72)$	$(9.7, 7.3)$

Table 1
Image sizes and effective sample resolutions as a function of objective magnification. The image sizes are computed after a quadrant of 90×90 cm separator which is tuned to 0 eV electrons at emission.

3.2 Full Flux Operation

Considering the dominating on-axis aberration terms, $p_{x,y}\,\delta$, the resultant image size is proportional to the fractional energy spread, Δ_δ. If the separator is tuned to reference electrons with a zero emission energy, all electrons in the distribution will have a positive δ, yielding an unnecessarily large fractional energy spread. The impact of these chromatic aberrations can be reduced by minimizing the effective Δ_δ. This can be done by tuning the separator to a reference energy which somewhat equally splits the electron distribution into a group with a positive δ and another with a negative δ. A reasonable choice of the reference energy for incoming electrons is 20 keV + 5 eV, which partitions the total beam distribution into two equal portions in our emission model with a work function of 5 eV (see Subsection 3.1). We note that the resultant aberration is roughly halved (see Table 2).

3.3 Size of Separator

The first separator prototype was designed with a transverse dimension of 90×90 cm and a vertical gap of 10 mm. For a reasonable magnification of $-20\times$, this separator had a large on-axis aberration term $p_y\delta$ which limited

the on-axis vertical sample resolution to 3.7 nm (see Table 1), exceeding the design requirement. We recognize that the on-axis aberration of a separator scales with the size of the magnet. Consequently, separators with scaled-down physical dimensions but with a proportionally scaled-up magnetic field value have reduced on-axis aberrations. A drawback of this approach is an increased beam filling factor, for the same beam distribution occupies relatively more transverse space in a scaled-down separator. This results in increased off-axis aberrations. As a compromise, we designed a second separator prototype with reduced transverse dimensions of 28 cm and a relatively enlarged vertical gap of 7 mm. It is worth pointing out that we have intentionally chosen the same physical dimensions for the 2nd PEEM3 separator prototype as the SMART separator so that meaningful comparisons can be made. Besides the aberration concerns, a scaled down separator magnet is also easier to align and is expected to have better long-term stability during operation.

Separator Setup	Location on sample (μm)	Sample Resolution X (nm)	Sample Resolution Y (nm)
Goals:			
1 μm field of view		< 1	< 1
10 μm field of view		< 5	< 5
90 cm, $-20\times$, 0 eV	$(0, 0)$	0.85	3.74
90 cm, $-20\times$, 5 eV	$(0, 0)$	0.41	2.0
90 cm, $-20\times$, 5 eV	$(-0.5, -0.5)$	0.36	1.8
90 cm, $-20\times$, 5 eV	$(-5, -5)$	0.61	5.1
28 cm, $-20\times$, 5 eV	$(0, 0)$	0.2	0.75
28 cm, $-20\times$, 5 eV	$(-0.5, -0.5)$	0.2	0.76
28 cm, $-20\times$, 5 eV	$(-5, -5)$	0.49	3.7

Table 2
Effective sample resolutions for a simplified PEEM model which employs linear representations for the acceleration gap and objective lens and a nonlinear representation for one quadrant of the separator magnet using a 4th-order TPSA map. Two separator models are compared: one with physical dimensions: 90cm$\times$90cm$\times$10mm, the other, 28cm $\times$ 28cm $\times$ 7mm; the magnification of the objective lens is assumed to be $-20\times$, and separator is tuned to either 0 eV of 5 eV electrons at emission.

3.4 Field-Size Dependent Resolution

The on-axis resolution of PEEM3 is determined by aberration terms which only depend on angular and energy spread of the beam. The off-axis resolution,

on the other hand, also depends on aberration terms which are functions of transverse positions. Consequently, the resolution of the PEEM system varies across the field of view. This effect is referred to as the field-size dependent resolution of the system. We have studied the impact of separator aberrations on the field-size dependent resolution by computing the image sizes of a point source located at the corners of the field of view. For both 90 cm and 28 cm separators, the system resolution is rather uniform across the 1 micron field of view. However, the off-axis aberrations of the separator cause significant degradation of the system resolution at corners of a 10 micron field of view. Fig. 4 shows the image distribution of a point emission source located at $(-5, -5)$ microns in the field of view. The aberrations at corners of a 10 micron field of view are increased by a factor of 2.5 and 5 for 90 cm and 28 cm separators respectively.

We illustrate the field-size dependent resolution in a 90 cm separator by computing images for a word pattern "ALS" placed at various locations in the field of view. (see Fig. 5). The word pattern is roughly 15×40 nm in size and the vertical spacing between adjacent points is 5 nm. As expected, the image remains sharp when the object is located at the corner of a 1 micron field of view. However, the image is completely blurred at the corner of a 10 micron field of view due to the fact that at this location the vertical resolution of the system is degraded to 5.1 nm due to field-size dependent aberrations.

3.5 Comparison with SMART Separator

As shown in Table 2, the second separator prototype with a transverse dimension of 28 cm meets the design requirements for both on-axis and off-axis aberrations. This separator is designed to work with 20 kV electron beams and a frontend magnification of $-20\times$. The groove current in this separator is $I = 72.29$ A and the magnetic field in the gap is 259.6 Gauss.

Due to the identical physical dimensions between this PEEM3 separator prototype and the SMART separator, we can compare key design parameters and some of most important aberration terms between these two designs (see Table 3.) We notice that the groove current and magnetic field agree to a level of less than 0.2% and all listed aberration coefficients agree to about 2% or better with exceptions of $x_{\alpha\beta\beta}$. Considering the fact that completely different field models and optics models have been used for designing these two separators, the remarkable agreement shown here provides strong evidence to validate both the SMART and PEEM3 separator optics designs. It is worth pointing out the observed relatively large discrepancies for non-critical aberration terms, $x_{\alpha\beta\beta}$ and $y_{\alpha\alpha\beta}$, in fact, indicate the limitation of the 2D magnetic field model used in PEEM3 separator design. For the PEEM3 separator, $x_{\alpha\beta\beta}$

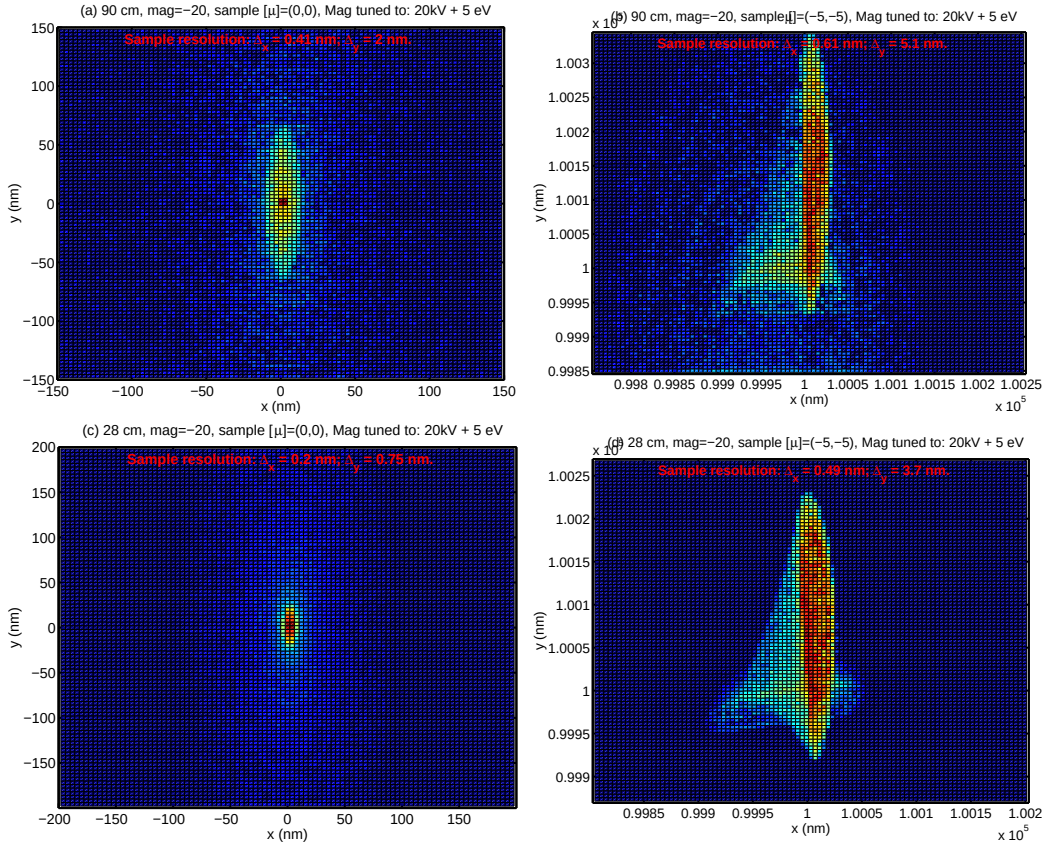

Fig. 4. Point emission source images both on-axis and off-axis at a corner of a 10 micron field of view after a quadrant of the separator. (a) 90 cm separator, the emission source is at $(0, 0)$ μm in the field of view; (b) 90 cm separator, the source is at $(-5, -5)$ μm; (c) 28 cm separator, the source is at $(0, 0)$ μm; (d) 28 cm separator, the source is at $(-5, -5)$ μm.

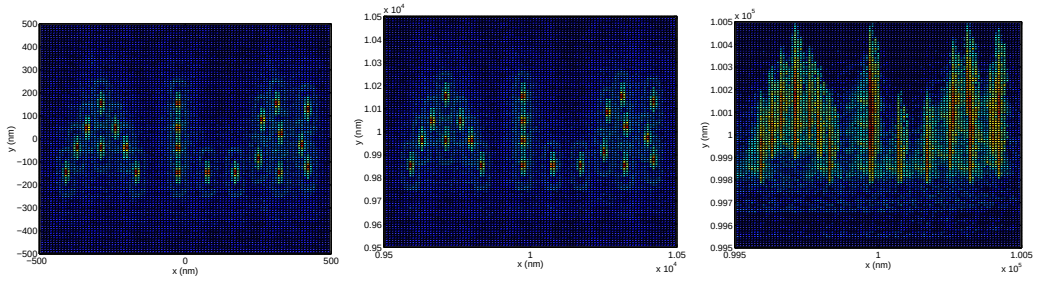

Fig. 5. Computed images for a word pattern, "ALS", located at various spots in the field of view. The images are computed after a quadrant of the separator with a linearized frontend. The vertical spacing among adjacent points is 5 nm on the sample plane. From the left to the right: (a) the pattern is centered at $(0, 0)$ μm in the field of view; (b) at $(-0.5, -0.5)$ μm; (c) at $(-5, -5)$ μm.

differs from $y_{\alpha\alpha\beta}$ by 4%, which indicates a certain level of violation of the symplectic condition.

Separator Comparison	PEEM3 (20 kV)	SMART (15, 20) kV	Difference
groove I [A]	72.39	62.3, 72.28	0.15%
field B [Gauss]	259.6	224, 259.9	−0.12%
$x_{\alpha\kappa}$	−0.084	−0.083	1%
$y_{\beta\kappa}$	−0.306	−0.300	2%
$x_{\alpha\alpha\alpha}$	0.071	0.071	$< 1\%$
$y_{\beta\beta\beta}$	5.9	5.9	$< 1\%$
$x_{\alpha\beta\beta}$	−0.362	−0.380	−5%
$y_{\alpha\alpha\beta}$	−0.374	−0.380	−2%

Table 3
Comparison of key design parameters and on-axis aberration coefficients between the 28 cm PEEM3 separator prototype and SMART separator. Note that the published SMART separator groove current and magnetic field are for 15 kV electron beams. Scaled SMART separator current and field values are used for comparison.

4 Analyses of Mechanical Misalignment

In the previous section, we have seen that a perfect 28 cm beam separator as designed would meet the resolution performance goals of PEEM3. In reality, various imperfections such as mechanical misalignments can have significant impact on the system resolution. In this section, we study how the mechanical misalignments can alter the separator aberrations and what can be done to effectively compensate for them.

The misalignment of the top and bottom halves of the separator is very difficult to model and analyze. Consequently, we decide to adopt a practical approach to minimize this type of misalignment in the mechanical design. We are considering partitioning the magnetic field areas into several localized pieces so that top and bottom halves can be machined together and pre-aligned with high precisions before being installed in the separator. With such care paid to manufacturing and aligning the critical magnetic surfaces vertically, we expect that the vertical misalignment of the separator will have less significant impact on the separator performance comparing to the horizontal misalignment.

Fig. 6 shows the design trajectory of the electron beam and the reference local coordinate system. The two horizontal directions are denoted as u and v respectively and the horizontal rotation angle of the groove is denoted as ϕ. There are a total of twelve grooves whose horizontal positions and angles can be misaligned. Besides the usual five differential algebra (DA) variables for beam dynamics, (x, p_x, y, p_y, δ), a total of 36 additional DA variables for groove positions and angles are used in the TPSA map with misalignment. Like in the previous studies, 4th order TPSA maps are used. However, since the amplitudes of various misalignments are small, we only keep the aberration terms which are either independent of or linearly dependent on the misalignment variables.

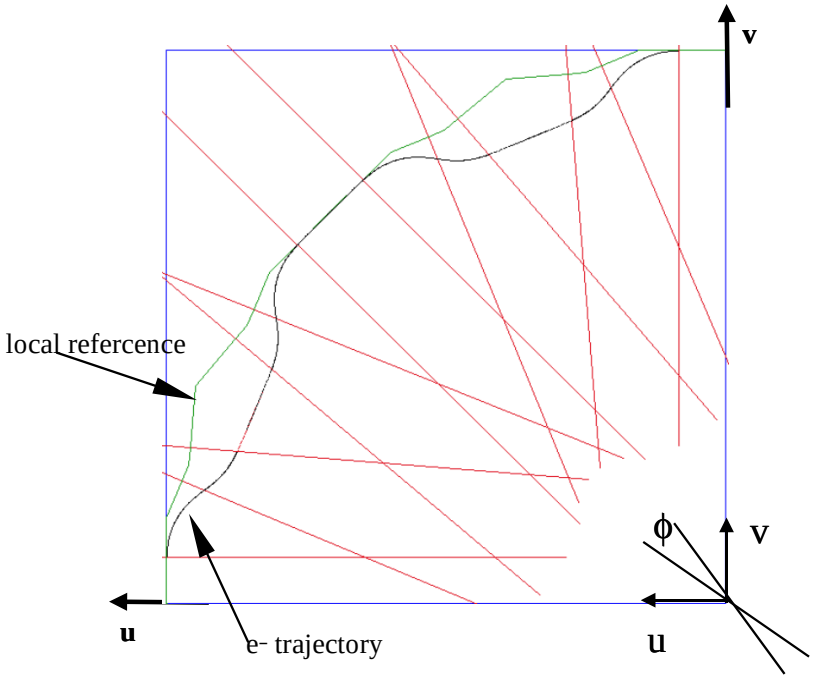

Fig. 6. The layout of the electron design trajectory in the mid-plane (horizontal plane) of the 28 cm beam separator magnet. Two horizontal directions are denoted as u and v directions and the horizontal rotation angle as ϕ.

4.1 On-axis Case

In this study, a set of reasonable alignment errors are set for separators: $\sigma_{u,v} =$ 25 microns for positions and $\sigma_\phi = 1$ mrad for the rotation angle. A 1 mrad rotation of the straight piece of the groove corresponds to about 25 micron changes in the end positions of the groove. Using a random number generator, we generate a set of Gaussian errors in position and angle with a 2σ cut. An ensemble of misaligned separators are then generated. We again compute and analyze the electron beam distribution after a quadrant of the separator on the image plane.

Fig. 7(a) and (c) show two images of a point emission source after misaligned separators with two different seeds for alignment errors. The horizontal image size in Fig.7(a) and the vertical image size in Fig.7(c) are increased by 20 times or more as compared with that of an ideal separator. Further investigations show that the increase of the separator aberration is mainly due the mismatch of the linear optics. By correcting both the linear focusing and dispersion in or around the separator, we are able to restore the level of aberrations to that of an ideal separator as shown in Fig.7(b) and Fig.7(d). In fact, Fig.7(a) is dominated by linear focusing errors in both horizontal and vertical directions while Fig.7(b) is the result of a large focusing error in the vertical direction and a large uncompensated horizontal dispersion.

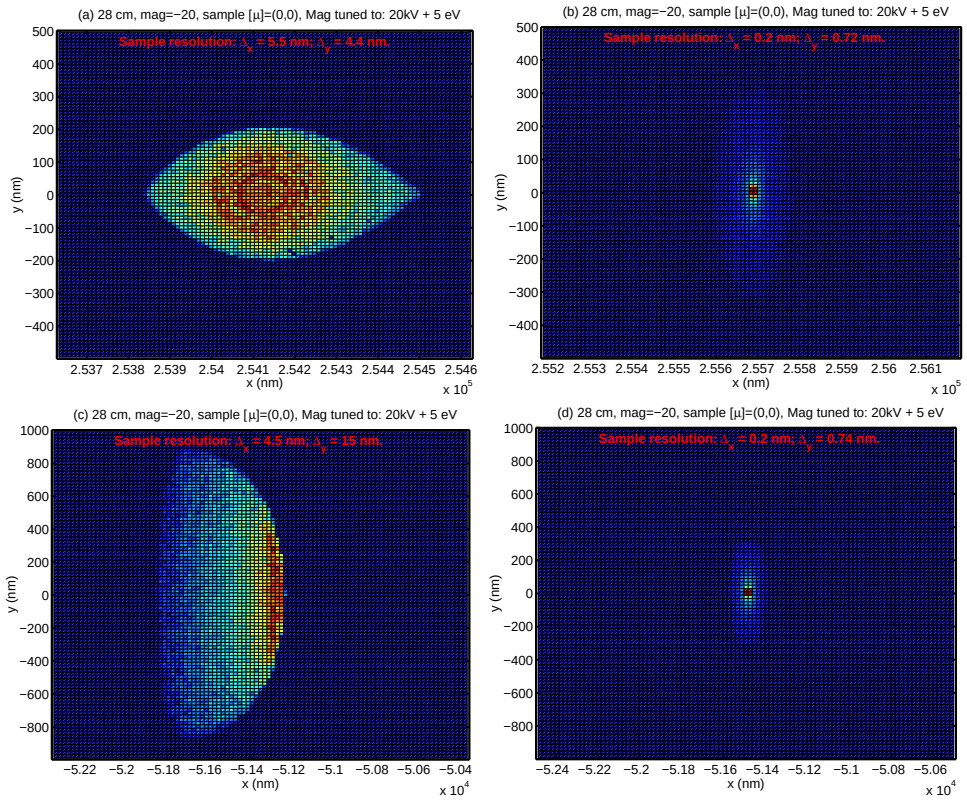

Fig. 7. Effectiveness of linear focusing and dispersion corrections for restoring the on-axis resolution for the 28 cm separator with alignment errors: $(\sigma_u, \sigma_v, \sigma_\phi) = (25\mu\text{m}, 25\mu\text{m}, 1\text{ mr})$. (a) the image of a point source with an error seed A, before correction; (b) with an error seed A, after correction; (c) with an error seed B, before correction; (d) with an error seed B, after correction;

An ensemble of 20 separators with random alignment errors have been studied systematically for the effectiveness of the linear corrections. The effective sample resolutions before and after the corrections are shown in Fig. 8 for the 28 cm separator. Comparing with the 0th case of an ideal separator, linear focusing corrections and dispersion corrections have successfully restored the aberration performance of all 20 misaligned separators.

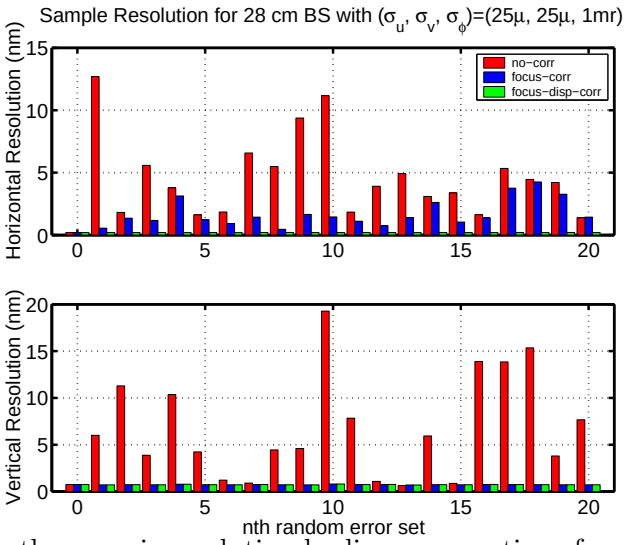

Fig. 8. Restoring the on-axis resolution by linear corrections for an ensemble of 20 separators with different sets of random errors. Note that we also plot the resolution of an ideal separator without alignment errors as the 0-th case.

4.2 Off-axis Case

The same ensemble of 20 misaligned separators are analyzed for the off-axis resolutions where the source point is located at a corner of a 10 micron field of view. Again, we observed significant increases in off-axis aberrations due to misalignment. After applying the same set of linear corrections as for the on-axis case with the same set of alignment errors, we are able to restore the off-axis resolution of the system to the similar level as that with an ideal separator (see Fig. 9).

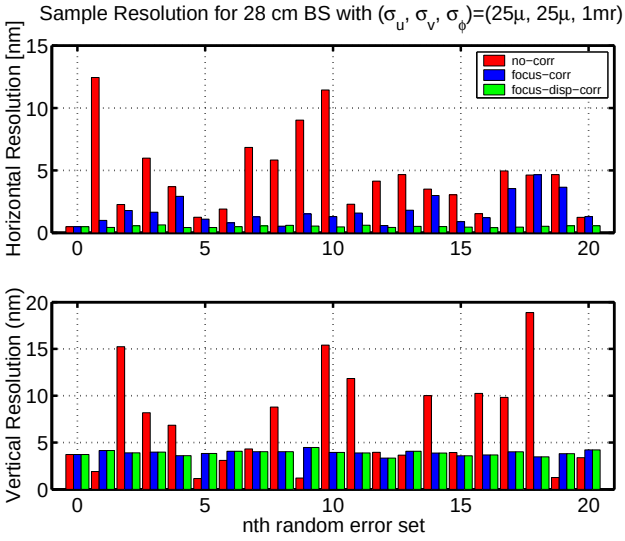

Fig. 9. Restoring the off-axis resolution at a corner of a 10 μm field of view by linear corrections for an ensemble of 20 separators with different sets of random errors. Note that we also plot the resolution of an ideal separator without alignment errors as the 0-th case.

4.3 Significance of Linear Corrections

It is important to point out that for any set of alignment errors with RMS strengths, $(\sigma_x, \sigma_y, \sigma_\phi) = (25\mu\text{m}, 25\mu\text{m}, 1\text{ mr})$, the only necessary corrections to restore the performance of a misaligned separator are linear focusing corrections and dispersion corrections. This observation has a couple of profound consequences:

(1) correctors for linear optics can be flexibly located either inside or outside the separator. In fact a correction scheme combining correctors inside and outside the separator can also work;
(2) the commissioning of the correction system can be greatly simplified – the resolution improvement can be made via the correction of the linear optics, for example, by measuring and restoring line distortions (using straight or curved lines) of the image. This is a much more effective procedure compared with the method which involves direct measurements of the image resolution, a very difficult and time-consuming task to perform.

It is also worth pointing out that the linear corrections work quite well to restore the separator performance for RMS alignment errors as large as $(\sigma_u, \sigma_v, \sigma_\phi) = (100\mu\text{m}, 100\mu\text{m}, 4\text{mr})$.

5 Summary

We have developed magnetic field and charged particle optics models for designing beam separator magnets for aberration compensated PEEMs. Prototype separator optics have been developed and their on-axis and off-axis aberrations have been analyzed under various operation conditions. A separator prototype with a physical dimensions, 28cm × 28cm × 7mm, has been identified to have adequate aberration performance for PEEM3. Analyses on mechanical alignment tolerance of this prototype magnet have demonstrated that linear optics corrections are effective to restore the separator performance for the level of misalignments expected in the manufacturing and installation of the device.

We are in the process of finalizing the separator optics. It is expected that the separator optics may further evolve as a result of optimizing its mechanical/electrical design. In addition, the final operation parameters of the frontend system may be different from the values assumed in this study. For example, we are anticipating a reduced magnification of the object lens at $-15\times$ instead of $-20\times$ as used in this study. Many of the analyses carried out in this work will be repeated for the final design of the separator.

In addition, besides mechanical tolerance, we plan to perform studies on cur-

rent variations of the triple coils in order to determine whether to individually feed the coils or to feed three coils in series plus additional secondary correction coils. We also plan to perform an integrated study of the PEEM3 performance by putting together nonlinear optics models for the frontend, separator, and correction mirror. Following these studies, the first prototype separator will then be built for rigorous bench tests.

Acknowledgment

We would like to thank Mike Scheinfein at Arizona State University for useful discussions on an earlier version of the separator magnet design.

References

[1] E. Bruche, Z. Phys. *8*6, 448 (1933).

[2] O. H. Griffith and W. Engel, Ultramicroscopy *3*6, 1 (1991).

[3] S. Anders, H. A. Padmore, R. M. Duarte, T. Renner, T. Stammler, A. Scholl, Rev. of Sci. Instr., vol 70, no. 10, p. 3973 –3981 (1999).

[4] Joachim Stohr, et. al., "High Resolution X-Ray Spectro-Microscopy Facility at the Advanced Light Source", DOE proposal, 2000.

[5] R. Fink, M. R. Weiss, E. Umbach, D. Preikszas, H. Rose, *et. al*, J. Electron Spectroscopy, no. 84, p. 231–250 (1997).

[6] R. Wichtendahl, R. Fink, H. Kuhlenbeck, D. Preikszas, H. Rose, *et. al*, Surface Review and Letters, Vol. 5, No.6, p. 1249–1256 (1998).

[7] H. Muller, D. Preikszas, H. Rose, J. Electron Microscopy, no. 48(3), p. 191–204 (1999).

[8] D. Preikszas, H. Rose, J. Electron Microscopy, no. 1, p. 1–9 (1997).

[9] M. Berz, Nucl. Instr. and Meth. A258, p. 431–436 (1987).

[10] M. Berz, Particle Accelerators, V. 24, p. 109 – 124 (1989).

[11] E. Forest, the full polymorphic package (FPP), an overloaded TPSA package, 2001.

[12] B. P. Tonner, D. Dunham, Nucl. Instr. and Meth. A347, p. 436–440 (1994).